Journal of Biomedical Optics

SPIEDigitalLibrary.org/jbo

Beyond the lateral resolution limit by phase imaging

Yann Cotte
M. Fatih Toy
Christian Depeursinge

Journal of Biomedical Optics 16(10), 106007 (October 2011)

Beyond the lateral resolution limit by phase imaging

Yann Cotte, M. Fatih Toy, and Christian Depeursinge
Ecole Polytechnique Fédérale de Lausanne (EPFL), Microvision and Microdiagnostics Group (MVD), Lausanne, 1015, Switzerland

Abstract. We present a theory to extend the classical Abbe resolution limit by introducing a spatially varying phase into the illumination beam of a phase imaging system. It allows measuring lateral and axial distance differences between point sources to a higher accuracy than intensity imaging alone. Various proposals for experimental realization are debated. Concretely, the phase of point scatterers' interference is experimentally visualized by high numerical aperture (NA = 0.93) digital holographic microscopy combined with angular scanning. Proof-of-principle measurements are presented by using sub-wavelength nanometric holes on an opaque metallic film. In this manner, Rayleighs classical two-point resolution condition can be rebuilt. With different illumination phases, enhanced bandpass information content is demonstrated, and its spatial resolution is theoretically shown to be potentially signal-to-noise ratio limited. [DOI: 10.1117/1.3640812]

Keywords: point spread function; microscopy; super-resolution; digital holography; phase imaging; phase vortices.

Paper 11165PR received Apr. 4, 2011; revised manuscript received Jul. 29, 2011; accepted for publication Aug. 29, 2011; published online Oct. 7, 2011.

1 Introduction

The limit of resolution is generally expressed by Rayleigh's criterion of resolution given by

$$d_{\min} = \alpha \frac{\lambda}{\mathrm{NA_{MO}}}, \tag{1}$$

limited by microscope objective's numerical aperture $\mathrm{NA_{MO}}$ and optical wavelength λ. Coherently illuminated imaging systems scale in Eq. (1) with a factor of $\alpha_{\mathrm{coh}} = 0.82$. Therefore, they suffer from an inferior lateral resolution compared to their incoherent counterpart $\alpha_{\mathrm{incoh}} = 0.61$.[1,2]

On the other hand, coherent imaging is an attractive research tool in many fields of biological research.[3] Techniques such as digital holographic microscopy (DHM) have the capability of imaging amplitude and quantitative phase simultaneously.[4] Consequently, the method is marker-free, noninvasive regarding the light intensity, and only camera acquisition rate limited.

Many attempts have been made to overcome a shortage in resolution power of coherent imaging systems. The general approach consists in exploiting unused degrees of freedom.[5] Following that idea, interference of spherical waves can be used to create phase vortex arrays.[6,7] Recently, the significance of such phase singularities for resolution has been demonstrated.[8] Following, it has been outlined how to fully exploit bandpass information content and how to directly improve coherent imaging system resolving power.[9]

The purpose of this paper is to investigate the principal lateral and axial resolution limits which can be related to the occurrence of asymmetric singularities in phase. Based on this observation, we elaborate concepts for coherent resolution beneath Abbe's limit [$\leq \lambda/(2\mathrm{NA_{MO}})$] with high-$\mathrm{NA_{MO}}$.

Address all correspondence to: Yann Cotte, EPFL, SCI-STI-CHD, BM 4118, station 17, Lausanne, Vaud 1015 Switzerland; Tel: 0041762032075; Fax: 0041216933701; E-mail: yann.cotte@a3.epfl.ch.

2 Asymmetric Phase Singularities

The destructive interference between waves emitted from point-scatterers results in phase singularities. Such discontinuities occur at spatial positions where the spherical waves emitted from each hole are out of phase. As reported earlier,[8] the orientation angle θ of those lines of singularities varies systematically with the point-scatters' pitch η. Our experimental realization of point-scatterers is depicted in Fig. 1(a), whereas Fig. 1(b) shows schematically their phase response in an image plane. A total of four destructive interferences are possible for the two pairs of rings. The characteristic spacing s between two out of phase circles, r_1 and r_2, i.e., with phase difference $\Delta\Phi = \pi$, can be calculated by

$$s = \frac{\Delta\Phi}{k_{\max}} = \frac{\pi}{(2\pi/\lambda)\mathrm{NA_{MO}}} = \frac{\lambda}{2\mathrm{NA_{MO}}}, \tag{2}$$

with the maximal spatial frequency $k_{\max} = 2\pi/\lambda$ allowed by $\mathrm{NA_{MO}}$. Following, our theoretical description is based on the experimental situation of an arbitrary phase difference $\Delta\phi$ between both emitters. In the case of $\Delta\phi \neq 0$, for instance through a longitudinal displacement Δz, a path difference $\Delta s = \lambda\Delta\phi/(2\pi)$ is introduced in $r_2 = r \pm \Delta s + s$ ("+," advanced phase; "−," retarded phase) relative to $r_1 = r$. Hence, Eq. (2) transforms into the effective spacing

$$s_\pm = s \pm \Delta s = s(1 \pm \mathrm{NA_{MO}}\Delta\phi/\pi), \tag{3}$$

which can be contracted or dilated. Combining the geometrical relations of Fig. 1 and solving them for η results in[8]

$$\eta(\theta_\pm, r, s_\pm) = \left\{2r^2 + 2rs_\pm + s_\pm^2 - \left[4r^2(r+s_\pm)^2 - s_\pm^2(2r+s_\pm)^2\cot^2\theta_\pm\right]^{1/2}\right\}^{1/2}, \tag{4}$$

with the angle $\theta_\pm$ relative to the symmetry axis and effective spacing $s_\pm$ defined by Eq. (3). For the same pitch η, Eq. (4) must

1083-3668/2011/16(10)/106007/6/$25.00 © 2011 SPIE

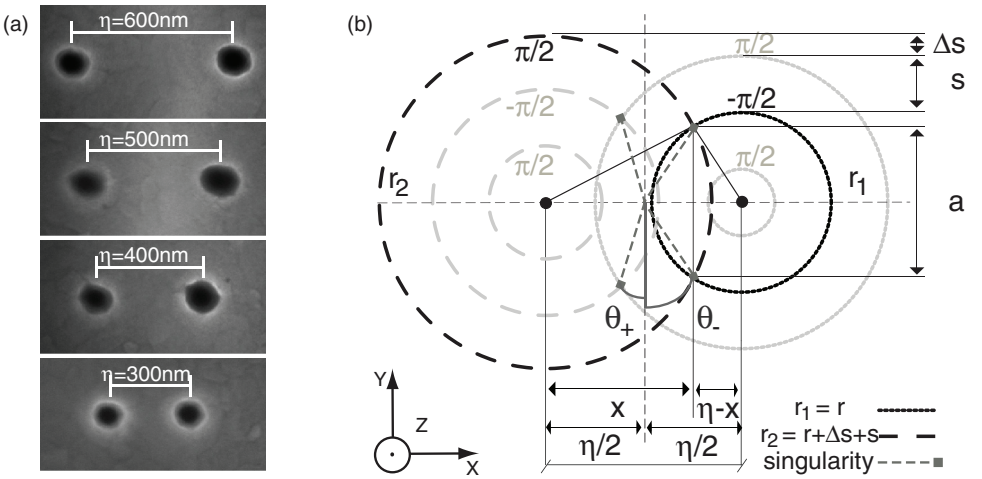

Fig. 1 In (a), SEM images of pair of nanoholes drilled by FIB in aluminum film at 100, 000× magnification. The images show nominal center-to-center pitches η of 600, 500, 400 and 300 nm with according scale bars. In (b), schematic illustration of image plane in phase with $\Delta\phi \neq 0$. Circles show contours of equal phase emitted from two point sources located in the circles' centers.

yield individually to pairs of asymmetric singularities summarized in Eq. (5):

$$\eta(\theta_+, r, s_+) \stackrel{!}{=} \eta(\theta_-, r, s_-). \tag{5}$$

Consequently, $\Delta\phi$ dephased point-scatterers feature asymmetric phase singularities oriented along $\theta_\pm$. The phase difference $\Delta\phi$ may offer advantages concerning the lateral as well as axial resolution, as discussed in Sec. 2.1 and Sec. 2.2.

2.1 *Axial Resolution*

A longitudinal displacement Δz of one of the point-scatterers results in an offset phase difference

$$\Delta\phi_{\text{long}} = \frac{2\pi n_m \Delta z}{\lambda}, \tag{6}$$

giving rise to $s_\pm$ according to Eq. (3) in mounting medium of refractive index n_m. By inverting Eq. (4), we can predict the angular dependence caused by Eq. (6):

$$\theta_\pm[\eta, r, s_\pm] = \arctan\left(s_\pm(2r + s_\pm)\left\{(s_\pm^2 - \eta^2)\left[\eta^2 - (2r + s_\pm)^2\right]\right\}^{-1/2}\right). \tag{7}$$

Equation (7) is plotted for a constant η in Fig. 2(a). Pairs of singularities are symmetrically oriented in the case of $\Delta z = 0$. Asymmetry is introduced by the existence of $\Delta z \neq 0$, so that one pair of singularities' θ is decreased while the other pair's angle is increased. That dynamic holds up to Δz of 0.32λ, at which point θ_+ reaches $\pi/2$ and cannot be further increased. Therefore, Fig. 2(a) suggests a unique dynamic range of maximal 0.32λ as an upper limit. However, it also suggests that the minimal distinguishable axial displacement is only signal-to-noise ratio (SNR) limited by the read-out accuracy of the phase singularities' orientation. In Fig. 2(a), a statistical reading precision of $\sigma = 4$ deg (Ref. 8) is indicated, and the axial resolution limit reads 0.05λ.

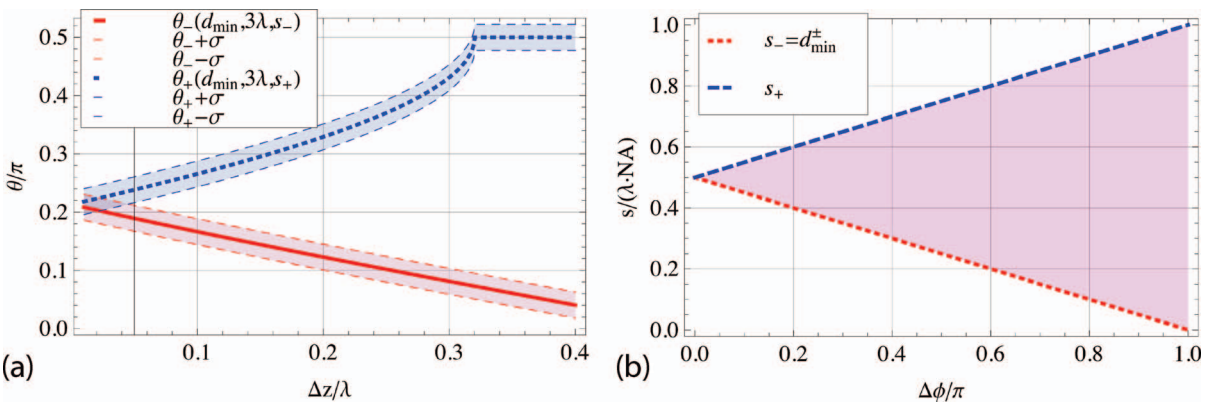

Fig. 2 Illustration of theoretical spatial resolution behavior based on asymmetric singularities. (a) Shows the singularities orientation with vertical precision $\sigma = 4$ deg versus a longitudinal displacement at a given distance $\eta = d_{\text{min,coh}}$. (b) Shows the dilated and contracted effective spacing as a function of the dephasing, whereby the latter one may be associated with $d^{\pm}_{\text{min}}$ of Eq. (9). The filled area indicates the advanced and retarded spacings' divergence.

Typically, that can be related with an axial precision of $\Delta z \approx 25$ nm at $\lambda = 532$ nm, $\eta = 400$ nm and $\mathrm{NA_{MO}} \approx 1$. Through several ring measurements, one can obtain such a statistical accuracy or better. On the other side, practical considerations, like discretization concerns or asymmetric aberrations,[8] might limit axial resolution.

2.2 *Lateral Resolution*

Given that θ can maximally reach $\pi/2$, Eq. (4) converges to

$$\lim_{\theta \to \pi/2} \eta = s_{\pm}, \tag{8}$$

stating that the minimal deducible distance η is limited by $s_{\pm}$. Thus, a new lateral resolution $d^{\pm}_{\mathrm{min}}$ limit is given for the maximal angle of θ:

$$d^{\pm}_{\mathrm{min}} = \min[\eta] = \min\left[\frac{\lambda}{2}\left(\frac{1}{\mathrm{NA_{MO}}} \pm \frac{\Delta\phi}{\pi}\right)\right]. \tag{9}$$

Equation (9) basically states Abbe's resolution limit from Eq. (1) ($\alpha_{\mathrm{Abbe}} = 0.5$) extended by an additive phase shift term. It results in resolvable distances that are in principle only SNR limited, as shown in Fig. 2(b), if $\Delta\phi$ is arbitrarily tunable. That implies that two point-scatterers at distances well beneath Abbe's resolution limit result in two asymmetric pairs of phase singularities. If θ_{max} exceeds $\pi/2$, only three singularities exist. In that situation, criterions to avoid possible ambiguities would be necessary:

1. Broadening effects of phase singularities.[10,11]
2. Phase scanning methods, as discussed in Sec. 3.

Eventually Eq. (9) is based on the assumption that $\Delta\phi$ itself can be created without any limitation on its lateral extension. If, however, $\Delta\phi$ is created by tilt illumination as suggested by Fig. 3, the dephasing is a function of η as further discussed in Sec. 3.

3 Experiment

For the proof of principle, we use a test target consisting of a thin opaque aluminum film (thickness = 100 nm) on a conventional coverslip.[12,13] Nanometric apertures ($\oslash_{\mathrm{nominal}} = 80$ nm) are drilled by focused ion beam (FIB) milling in the coating and are placed at very close pitches η. The fabricated pitch is controlled and measured by scanning electron microscopy (SEM), as shown in Fig. 1(a). The different double hole series serve as experimental test targets. For phase imaging, a DHM setup in transmission configuration (cf. Fig. 3) is used. The light source is a neodymium-doped yttrium aluminium–garnet laser (Nd:YAG) at wavelength $\lambda = 532$ nm. The DHM setup is equipped with a microscope objective, $63 \times \mathrm{NA_{MO}} = 0.93$ (in air) in combination with an additional relay magnification to reach a lateral sampling δx of 80 nm. The condenser lens' numerical aperture, called $\mathrm{NA_{cond}}$, is 0.25.

It is difficult to experimentally realize exact and small axial displacements Δz of one hole relative to another. Instead, we present a proof-of-principle measurement of the impact of $\Delta\phi$ on lateral resolution. The phase difference $\Delta\phi$ is created by a wedge prism which is put in imaging condition with respect to the sample by a 4-f system, shown in Fig. 3. The incident angle α can maximally reach the steepest angle allowed by $\mathrm{NA_{cond}}$ used to excite the point-scatters. Hence, the phase difference

$$\Delta\phi_{\mathrm{lat}} = \frac{2\pi n_m \eta \sin\alpha}{\lambda}\cos\beta, \tag{10}$$

where α is defined by the condenser lens $\alpha = \arcsin(\mathrm{NA_{cond}}/n_m)$, without mounting medium ($n_m = 1$). The rotation angle β of the wedge prisms in Eq. (10) serves to tune $\Delta\phi$. The maximal singularities' asymmetry is reached at $\beta = [0, \pi]$, whereas perpendicular $\beta = [\pi/2, 3\pi/2]$ holds for symmetric singularities configuration. By introducing Eq. (10) in Eq. (3), the effective spacing becomes NA limited by condenser and MO

$$s_{\pm} = \frac{\lambda}{2\mathrm{NA_{MO}}} \pm \eta \mathrm{NA_{cond}} \cos\beta. \tag{11}$$

Furthermore, the maximal condition for resolution in Eq. (8) states $s_{\pm} \leq \eta$. Thus, according to Eq. (9), the minimum of Eq. (11) yields for the resolution limit using tilt illumination

$$d^{+}_{\mathrm{min}} = \min[\eta] = \frac{\lambda}{2\mathrm{NA_{MO}}\,[1 + \mathrm{NA_{cond}}]}. \tag{12}$$

In a practical imaging system, the resolution limit can be estimated to reach minimally

$$\lim_{\mathrm{NA_{cond}} \to \max} \lim_{\mathrm{NA_{MO}} \to \max} d^{+}_{\mathrm{min}} \approx \frac{\lambda}{7.2}, \tag{13}$$

assuming a maximal possible immersion NA of about 1.46. With a short optical wavelength $\lambda = 400$ nm, the lateral limit with tilt illumination in Eq. (13) leads to $d^{+}_{\mathrm{min}} \approx 60$ nm.

4 Results

In Figs. 4(a), 4(c), and 4(k), and Figs. 4(g), 4(i), and 4(k) the phase singularities' behavior for tuning β is demonstrated with different pitches η. It can be seen that singularities' orientations can be indeed tuned by introducing a phase difference $\Delta\phi$ that is controlled by the wedge prism's orientation β, as defined in Fig. 3.

The phase singularities are symmetrically oriented for a perpendicular holes' excitation ($\beta = \pi/2$), shown in Fig. 4(c) for $\eta = 400$ nm and Fig. 4(i) for $\eta = 300$ nm. Both images show the phase map of distances η well beneath the Rayleigh resolution limit of $d^{\mathrm{Rayleigh}}_{\mathrm{min}} \approx 470$ nm. The pitch of image Fig. 4(c) is about Abbe's resolution limit of $d^{\mathrm{Abbe}}_{\mathrm{min}} \approx 300$ nm. Thus, four singularities are observable in Fig. 4(c), while they seem to merge to two broadened singularities in Fig. 4(i).

By detuning β, $\Delta\phi \neq 0$ can be controlled and the phase singularities become asymmetrically oriented. In the case of $\eta = 400$ nm, the two singularities merge on one side while opening up further on the opposed side. This results in a total of three singularities in Figs. 4(a) and 4(e). In the case of $\eta = 300$ nm, an originally merged singularity opens up again and consequently results in three singularities in Figs. 4(g) and 4(k).

The importance of the described behavior can be well observed in their spectra, depicted in Figs. 4(b), 4(d), and 4(f), and Figs. 4(h), 4(j), and 4(l). The Fourier-transform leads to a mixing up of modulus and phase of the complex image. Thus, the real space phase singularities are seen as minimum transmittances in the amplitude k-space (wavenumber). Figures 4(d) and 4(j) visualize the significance of $d^{\mathrm{Rayleigh}}_{\mathrm{min}}$ and $d^{\mathrm{Abbe}}_{\mathrm{min}}$. At Abbe's resolution limit of $\eta = 300$ nm in Fig. 4(j), the minimal transmittances reach the bandpass's edges, which corresponds to a wavenumber content of $k \approx 2(2\pi/\lambda)$.

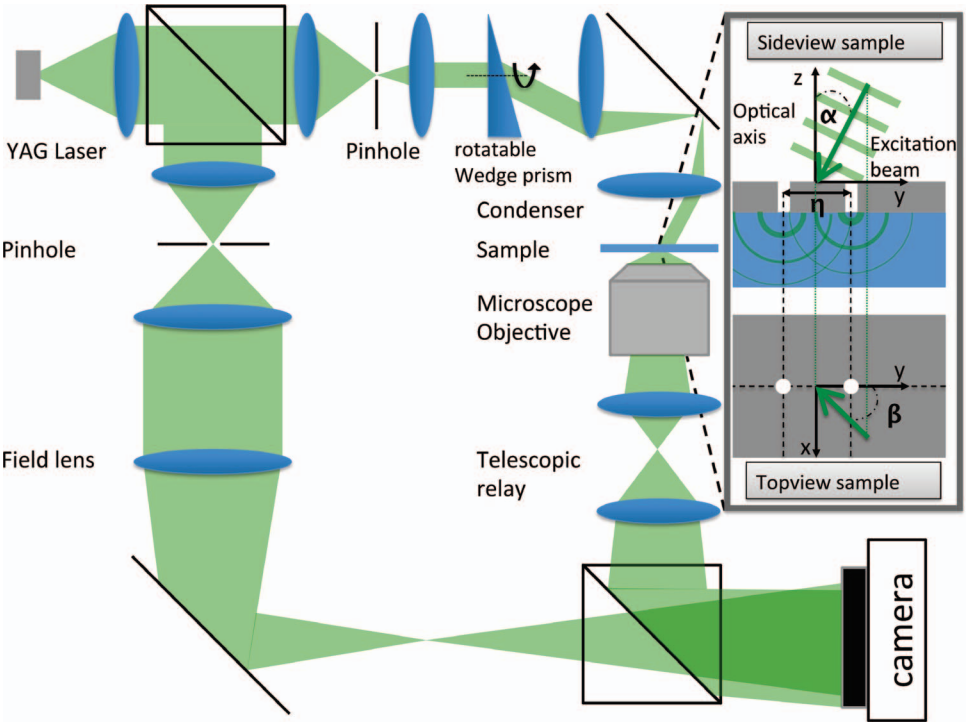

Fig. 3 Scheme of experimental setup. In DHM transmission configuration, a rotatable wedge prism is used to tune illumination conditions. The inset illustrates excitation beam's orientation in side and top perspective of the test target [cf. Fig. 1(a)]. The beam propagates in the direction of β (green arrow: k-vector) and is inclined by angle α.

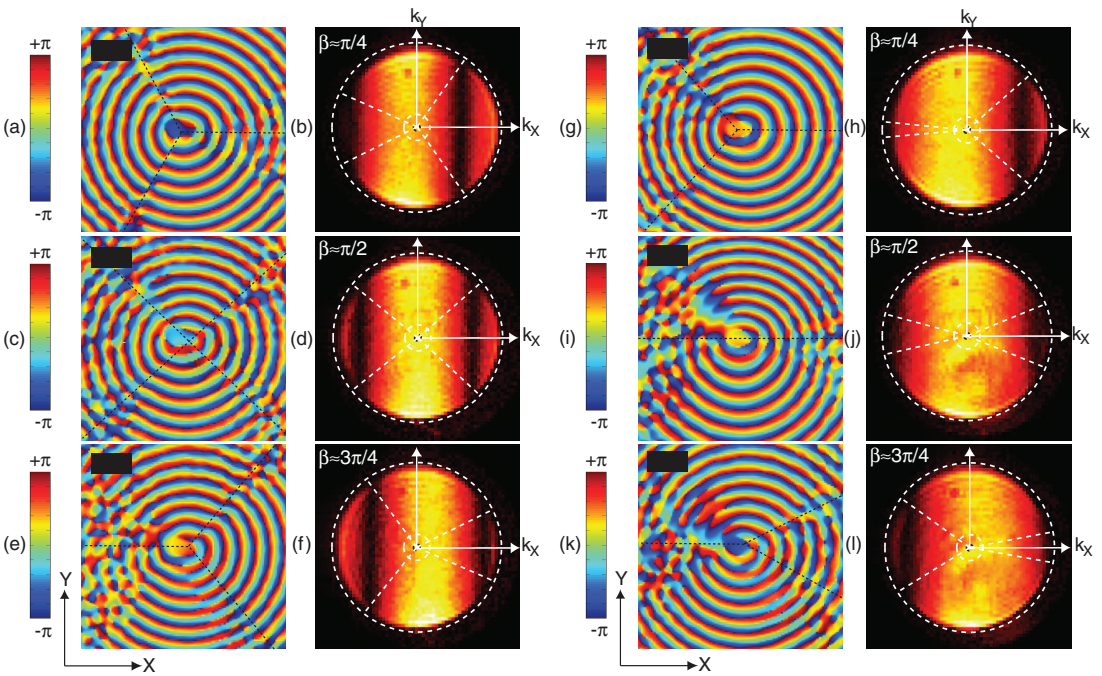

Fig. 4 Proof-of-principle measurements. The test target [cf. Fig. 1(a), $\eta = 400$ nm] is shown in phase images (a), (c), and (e) for different wedge prism orientations $\beta = [\pi/4, \pi/2, 3\pi/4]$, according to Fig. 3. The scale bar is 2μm$\times 1\mu$m and the black stroke lines indicate the idealized singularities. Additionally, the log-amplitude spectra of the complex fields are shown in images (b), (d), and (f) for the respective β values, including the spectrally measured $\theta_{\pm}$ angles (white dashed lines). Images (g)–(l) show the according phase images and amplitude spectra for $\eta = 300$ nm of Fig. 1(a).

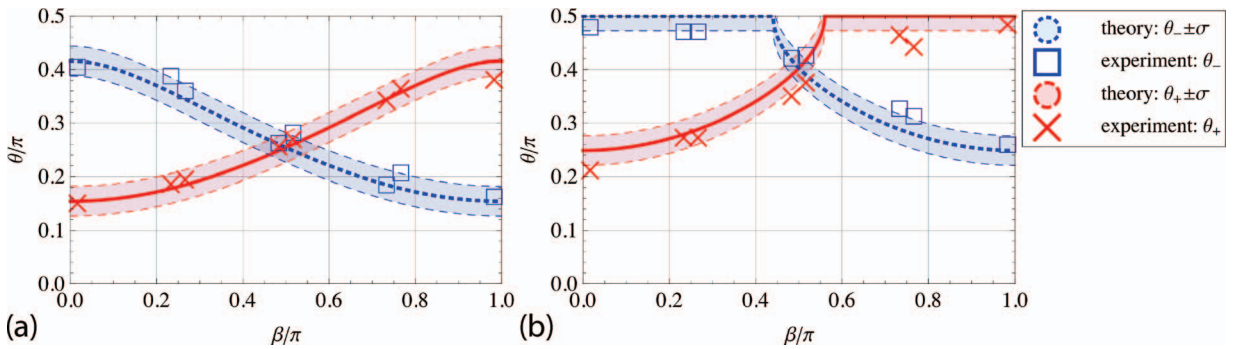

Fig. 5 Comparison of theory and experiment. For $\eta = 400$ nm, the experimental $\theta_{\pm}$ [cf. Figs. 4(a)–4(f)] are plotted in graph (a), together with theoretical curves given by Eqs. (7) and (11). Additionally, a vertical region of trust of $\sigma = 5$ deg is indicated. In graph (b), the same comparison is shown for $\eta = 300$ nm of Figs. 4(g)–4(l).

The transmittances minima shift asymmetrically to different frequencies as β is detuned, yielding for $\Delta\phi \neq 0$. As observed in Fig. 4, their positions shift on one spectral side to lower and on the other spectral side to higher wavenumbers k_x. In this manner, higher frequencies that are originally not allowed by the bandpass can be accessed. Eventually, it gives rise to resolution beneath Abbe's limit. The maximal shift of the transmittances minima in Fig. 4 corresponds to the largest angle θ of the phase singularities.

The comparisons of real-space with its corresponding spectra reveal that θ can be more precisely assessed in k-space. For instance, one can see that the three singularities in phase image Fig. 4(a) correspond actually to four singularities in k-space. In real space, this behavior is barely observable due to broadening effects.[10,11]

For the following analysis, the angle θ is directly measured from the spectra in Fig. 4 and results are visualized in Fig. 5. It compares the experimental values of θ directly to the theory of Eqs. (7) and (11). Nonzero phase shifts, i.e., $\beta \neq \pi/2$, lead to a splitting up of singularities' orientation $\theta_{\pm}$. In Fig. 5(a), angles $\theta_{\pm}$ never exceeds the maximal orientation of $\theta = \pi/2$. Contrarily, in the case of Fig. 5(b), the saturation point is already reached by little detuning of β. It features only three singularities over a large β-range. The experimentally observed behavior follows the theoretical prediction within the angular precision, both illustrated in Fig. 5.

5 Discussion

The test target of Fig. 1(a) has been especially designed to analyze the resolving power of phase imaging. It allows direct proof-of-principle measurements and demonstrates the practical role of coherent cross-talk in phase imaging. In a more general view, any nontransparent object could be thought to be composed of a three-dimensional distribution of scatterers, thus resulting in coherent cross-talk. Since the presented method is based on interferometric phase imaging, the described effects are generally less dependent on a number of photons.[14] Even in the case of phase objects, the occurrence of phase singularities has been reported.[6]

The observation of phase singularities serves two purposes. On the one hand, it offers a direct method of measuring lateral and axial distance differences between point sources to a higher accuracy than intensity imaging alone. On the other hand, it allows to study the information content of any coherent imaging systems bandpass. In Sec. 4, k-space information content is demonstrated to be in accordance with Abbe's diffraction limit in configuration of Fig. 6(a). We propose the technique of complex deconvolution to fully exploit bandpass limited information content.[9]

To further increase bandpass' information content beyond Abbe's limitation, phase shifts $\Delta\phi$ can be introduced as summarized in Fig. 6(b) and Eq. (9). Experimentally, such conditions can be achieved for any sample by illumination beam scanning[15]

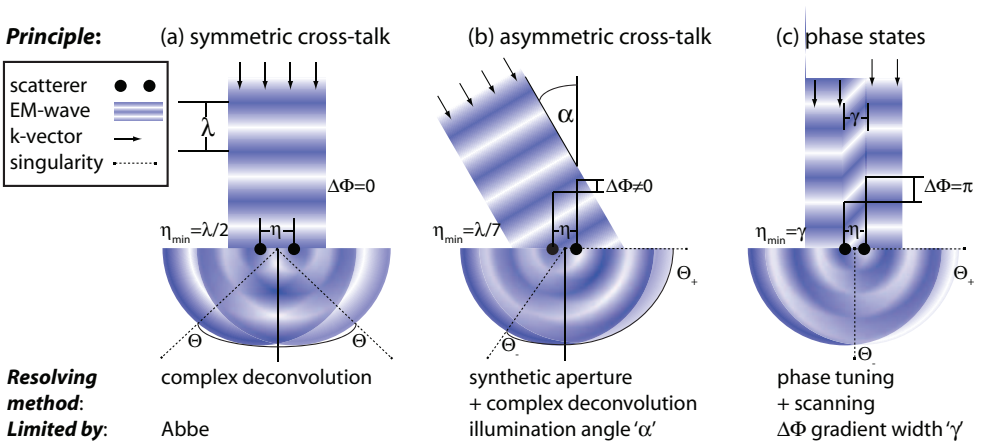

Fig. 6 Overview of concepts of lateral super-resolution techniques based on phase imaging.

or sample rotation.[16] Consequently, information content is increased and may be exploited by synthetic bandpass aperture[17] combined with complex deconvolution.[16] In this configuration, Eq. (10) teaches that resolution is limited by wavelength λ, tilting angle α, and scatterer's distance η.

However, following the idea of tuning $\Delta\phi$, Fig. 6(c) suggests how to overcome those limitations. We propose a tunable π-step phase scanning method, which results in maximal asymmetric singularity states. As known from STED or PALM-STORM, beam modulation patterns such as phase plates[18] or spatial light modulation[19] can be used to create first-order Bessel beams with line-singularities. Alternatively, also a "doughnut" mode beam intrinsically offers a steep π-step.[20] In this manner, the illumination beam itself can be used to scan through phase states and switch them dependently of sample's optical properties. The technique's resolution given by Eq. (9) should be, in principle, only limited by phase gradient's width γ, as seen in Fig. 6(c). If combined with DHM detection, a marker-free resolution well beyond $\lambda/7.2$ could be accessed, resulting in a new field of phase imaging applications for biological research.[21]

6 Concluding Remarks

Based on fundamental geometry and elemental physical considerations, resolution theory is extended for coherent imaging systems. Scatterer's relative axial displacement Δz leads to dephased signals. Their mutual interferences result in appearance of asymmetric singularities in phase, which yield highly sensitive axial resolution. Similarly, asymmetric singularities, caused by beam phase shifts $\Delta\phi \neq 0$, indicate improved lateral resolution. For this case, the bandpass' information content is experimentally demonstrated to be extended. The experimental proof confirms the correctness of derived theory. This theory offers an alternative explanation on how to improve resolution by angular scanning.[15] In conclusion, the lateral resolution limit can be extended by angular scanning techniques up to $\lambda/7.2$ and beyond by π-step phase scanning.

Acknowledgments

The author wants to acknowledge Swiss National Science Foundation (SNSF), Grant No. 205 320 – 130 543, for its financial support and the Center of MicroNano-Technology (CMI) for the cooperation on its research facilities.

References

1. M. Born and E. Wolf, *Principles of Optics* 6th ed., Cambridge University Press, Cambridge (1987).
2. S. V. Aert, D. V. Dyck, and A. J. den Dekker, "Resolution of coherent and incoherent imaging systems reconsidered: classical criteria and a statistical alternative," *Opt. Express* **14**, 3830–3839 (2006).
3. C. Depeursinge, P. Jourdain, B. Rappaz, P. Magistretti, T. Colomb, and P. Marquet, "Cell biology explored with digital holographic microscopy," in *Biomedical Optics*, OSA Technical Digest (CD), paper BMD58, Optical Society of America, Washington, DC (2008).
4. E. Cuche, P. Marquet, and C. Depeursinge, "Simultaneous amplitude-contrast and quantitative phase-contrast microscopy by numerical reconstruction of fresnel off-axis holograms," *Appl. Opt.* **38**, 6994–7001 (1999).
5. C. J. Sheppard, "Fundamentals of superresolution," *Micron* **38**, 165–169 (2007).
6. M. Totzeck and H. J. Tiziani, "Phase-singularities in 2d diffraction fields and interference microscopy," *Opt. Commun.* **138**, 365–382 (1997).
7. S. Vyas and P. Senthilkumaran, "Vortex array generation by interference of spherical waves," *Appl. Opt.* **46**, 7862–7867 (2007).
8. Y. Cotte, M. F. Toy, E. Shaffer, N. Pavillon, and C. Depeursinge, "Sub-rayleigh resolution by phase imaging," *Opt. Lett.* **35**, 2176–2178 (2010).
9. Y. Cotte, M. F. Toy, N. Pavillon, and C. Depeursinge, "Microscopy image resolution improvement by deconvolution of complex fields," *Opt. Express* **18**(19), 19462–19478 (2010).
10. N. Abramson, "The holo-diagram. vi: Practical device in coherent optics," *Appl. Opt.* **11**, 2562–2571 (1972).
11. N. Abramson, "Optical resolution and the duality of light," *Appl. Opt.* **47**, D1–D5 (2008).
12. H. F. Schouten, G. Gbur, T. D. Visser, and E. Wolf, "Phase singularities of the coherence functions in young's interference pattern," *Opt. Lett.* **28**, 968–970 (2003).
13. Y. Cotte and C. Depeursinge, "Measurement of the complex amplitude point spread function by a diffracting circular aperture," in *Focus on Microscopy, Advanced Linear and Non-Linear Imaging*, TU–AF2–PAR–D (2009).
14. F. Charrière, B. Rappaz, J. Kühn, T. Colomb, P. Marquet, and C. Depeursinge, "Influence of shot noise on phase measurement accuracy in digital holographic microscopy," *Opt. Express* **15**(14), 8818–8831 (2007).
15. M. Debailleul, V. Georges, B. Simon, R. Morin, and O. Haeberle, "High-resolution three-dimensional tomographic diffractive microscopy of transparent inorganic and biological samples," *Opt. Lett.* **34**, 79–81 (2009).
16. Y. Cotte, F. M. Toy, C. Arfire, S. S. Kou, D. Boss, I. Bergoënd, and C. Depeursinge, "Realistic 3d coherent transfer function inverse filtering of complex fields," *Biomed. Opt. Express* **2**(8), 2216–2230 (2011).
17. V. Mico, Z. Zalevsky, C. Ferreira, and J. García, "Superresolution digital holographic microscopy for three-dimensional samples," *Opt. Express* **16**, 19260–19270 (2008).
18. T. Watanabe, Y. Igasaki, N. Fukuchi, M. Sakai, S. ichi Ishiuchi, M. Fujii, T. Omatsu, K. Yamamoto, and Y. Iketaki, "Formation of a doughnut laser beam for super-resolving microscopy using a phase spatial light modulator," *Opt. Eng.* **43**(5), 1136–1143 (2004).
19. J. Leach, M. R. Dennis, J. Courtial, and M. J. Padgett, "Vortex knots in light," *New J. Phy.* **7**(1), 55 (2005).
20. O. Boyko, T. A. Planchon, P. Mercre, C. Valentin, and P. Balcou, "Adaptive shaping of a focused intense laser beam into a doughnut mode," *Opt. Commun.* **246**(1–3), 131–140 (2005).
21. P. Kanchanawong, G. Shtengel, A. M. Pasapera, E. B. Ramko, M. W. Davidson, H. F. Hess, and C. M. Waterman, "Nanoscale architecture of integrin-based cell adhesions," *Nature* **468**(7323), 580–584 (2010).